analytical chemistry

pubs.acs.org/ac Article

CuS QDs/Co_3O_4 Polyhedra-Driven Multiple Signal Amplifications Activated h-BN Photoeletrochemical Biosensing Platform

Jisui Tan, Bo Peng, Lin Tang,* Guangming Zeng,* Yue Lu, Jiajia Wang, Xilian Ouyang, Xu Zhu, Yu Chen, and Haopeng Feng

Cite This: *Anal. Chem.* 2020, 92, 13073−13083 Read Online

ACCESS | Metrics & More | Article Recommendations | Supporting Information

ABSTRACT: Herein, we developed an unmodified hexagonal boron nitride (h-BN) photoelectrochemical (PEC) biosensing platform with a low background signal and high sensitivity based on CuS quantum dots (QDs)/Co_3O_4 polyhedra-driven multiple signal amplifications. The prepared porous h-BN nanosheets with large specific surface areas, as the photoelectric substrate material, can provide extensive active reaction sites. Meanwhile, the CuS QDs/Co_3O_4 polyhedra were synthesized by the zeolitic imidazolate framework (ZIF-67) and utilized as a multiple signal amplifier, which can not only drive the p-n semiconductor quenching effect to compete with the h-BN photoelectrode for the consumption of electron donors and exciting light but also trigger a mimetic enzymatic catalytic precipitation effect to inhibit electron transfer. The quenching ability and peroxidase-like activity of CuS QDs/Co_3O_4 polyhedra were evaluated to prove its superiority, and the possible mechanisms of electron transfer and enzymatic catalytic were further analyzed in detail. The developed PEC biosensing platform for the chlorpyrifos assay presented outstanding performance with a wide linear range from 1×10^{-1} to 1×10^{7} ng mL^{-1} and a low detection limit of 0.34 pg mL^{-1} and exhibited excellent selectivity, reproducibility, and stability. In addition, the CuS QDs/Co_3O_4 polyhedra-activated h-BN PEC biosensing platform may exhibit universality for various analytes via replacing the corresponding target aptamer sequence. This work provides a remarkable inspiration and valuable reference for the development of the PEC biosensor, and the signal amplifier-enabled unmodified PEC biosensing platform strategy has a bright application in early safety warning, bioanalysis and clinical diagnosis.

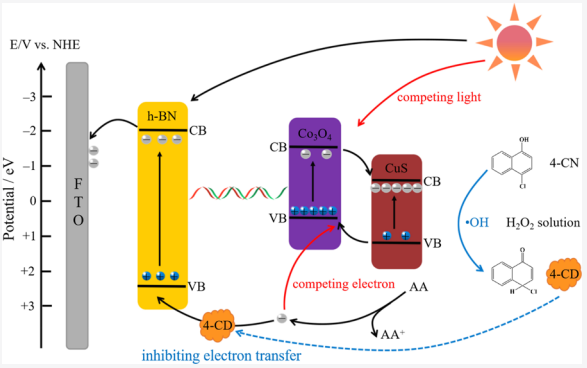

INTRODUCTION

Photoelectrochemical (PEC) bioanalysis, as an emerging analytical technology with extensive application potentials, has aroused tremendous attention due to its simple device, fast response, and excellent sensitivity.[1,2] Fundamentally, the PEC bioanalysis depends on the photocurrent signal change in the photoelectric conversion process, which involved the interaction between the photoelectrode and analyte under visible-light irradiation.[3] Therefore, excellent photoelectric materials play an important role in the performance of PEC bioanalysis. Common photoelectric materials, such as nanocrystalline materials and conducting polymer films, generally require complex modification, including element doping, construction of composite materials, and introduction of specific groups[4,5] because some shortcomings (low charge mobility, instability, poor biocompatibility, and hydrophilicity) may restrict the application of monomer materials.[3,6] Before that, most works generally focus on the complex modification of photoelectric substrate materials (especially the coupling of different materials) to enhance the performance of the PEC biosensing platform.[7,8] However, the formation of built-in electric field in complex materials can result in an increased background signal (caused by the increase of dark current), instability, and poor reproducibility of the sensing platform.[9] Therefore, it is of great significance to pursue an excellent photoelectric substrate material without modification for the development of the PEC biosensing platform with a negligible background signal and ultrahigh sensitivity.

Two-dimensional (2D) layered materials, including graphene, molybdenum disulfide (MoS_2), and graphitic carbon nitride (g-C_3N_4), have excellent stability, high charge mobility, large specific surface areas, and good biocompatibility[10] and are particularly advantageous to fabricate the PEC biosensing platform.[11,12] Hexagonal boron nitride (h-BN), as an n-type semiconductor with a 2D graphene-like framework, has wide

Received: May 9, 2020
Accepted: September 2, 2020
Published: September 2, 2020

https://dx.doi.org/10.1021/acs.analchem.0c02002
Anal. Chem. 2020, 92, 13073−13083

Scheme 1. Schematic Illustration of the PEC Biosensing Platform for the Chlorpyrifos Assay

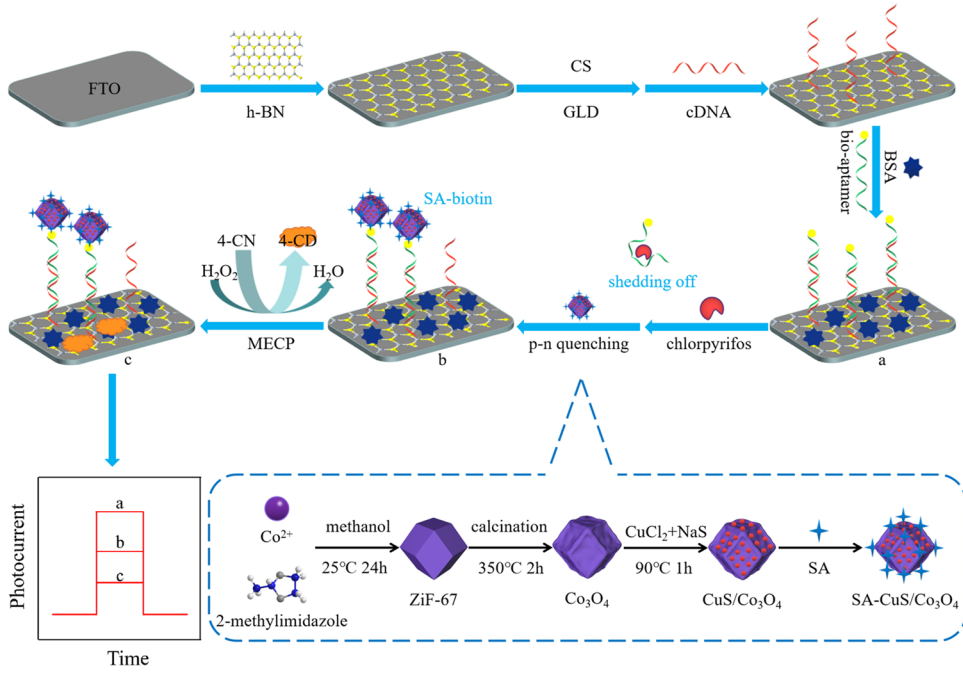

applications in photocatalysis,[13] drug delivery, and bioimaging.[14,15] Meanwhile, h-BN possesses good conductivity, large specific surface areas, and high charge carrier mobility, which can endow itself a good photoelectric conversion efficiency.[16] Furthermore, our previous work has first proven that h-BN is an excellent photoelectric substrate material for the application of the PEC biosensor.[17]

The signal amplification strategy is an effective method to develop a highly sensitive PEC biosensing platform and mainly includes a steric hindrance effect, energy transfer, p-n semiconductor quenching effect, and enzymatic reactions.[18,19] For the p-n semiconductor quenching-related PEC biosensors, the p-type semiconductor competes to expend electron donors and exciting light with n-type semiconductor, bringing about an obviously decreased photocurrent, which is emerging as a remarkable quenching effect. For instance, Yuan's group reported that PbS quantum dots (p-type) quench the fullerene-decorated AuNP@MoS_2 (n-type) PEC biosensor for ultrasensitive ATP detection.[20] Consequently, it is significant to investigate an effective p-type semiconductor nanomaterial as the quencher of the h-BN (n-type) PEC biosensing platform for signal amplification with excellent sensitivity.

The mimetic enzymatic catalytic precipitation (MECP) effect, as an effective signal amplification strategy, has received considerable attention since the generated insoluble precipitates can effectively hinder electron transfer.[21] Recently, various peroxidase-like nanomaterials, including carbon nanomaterials and transition metal oxides, exhibit excellent performance in enzymatic reactions.[22,23] Cobalt oxide (Co_3O_4), a p-type semiconductor with peroxidase-like activity, can oxidize 3,3,5,5-tetramethylbenzidine (TMB) to blue product under a hydrogen peroxide (H_2O_2) environment.[24] In addition, the zeolitic imidazolate framework (ZIF-67) contains cobalt ions linked by 2-methylimidazole ligands that can be used as a precursor to prepare ZIF-67-derived Co_3O_4 polyhedra, which has been reported with excellent photoelectric conversion performance in photocatalysis and biosensing applications because of its large specific surface areas.[25,26] Copper sulfide (CuS) is also a p-type semiconductor and has an excellent absorption of the full-light spectrum with a narrow band gap (about 1.8 eV).[27] Meanwhile, CuS also possesses the mimic nanozyme activity and can trigger the enzyme catalytic precipitation reaction for signal amplification.[28] Moreover, the quantum dot (QD) level nanomaterial exhibits the edge effects and defect centers for the further enhancement of photoelectric performance, such as MoS_2 QDs and CdSe QDs.[29,30] Based on the above mentioned points, these inspire us to synthesize a CuS QDs-modified Co_3O_4 polyhedra (CuS QDs/Co_3O_4 polyhedra) p-type heterojunction to drive the p-n semiconductor quenching effect and mimetic enzymatic catalytic precipitation strategy to endow the h-BN PEC biosensing platform with a low background signal and ultrahigh sensitivity.

Herein, by utilizing ZIF-67 dodecahedra as the precursor, the CuS QDs/Co_3O_4 polyhedra p-type heterojunction was prepared and utilized as a multiple signal amplifier to enable the h-BN biosensing platform. Experimentally, chlorpyrifos was selected as an analyte model for the PEC assay to reveal the superiority of the biosensing platform. As depicted in Scheme 1, the n-type semiconductor h-BN was utilized as the photoelectrode substrate material because of its good photoelectric conversion efficiency and large specific surface areas. After that, the amino-modified complementary DNA (cDNA) was anchored on the h-BN photoelectrode material surface due to the formation of amide bonds, and then, the aptamer-cDNA complexes were obtained by the DNA hybridization reaction. After being incubated with chlorpyrifos, the aptamer fell off from the electrode surface due to the strong affinity between the aptamer and chlorpyrifos. After washing to remove the unfixed aptamer-chlorpyrifos complexes, the streptavidin (SA)-labeled CuS QDs/Co_3O_4 polyhedra bioconjugate was introduced to the h-BN biosensing platform by specific binding of SA and biotin. Afterward, the p-type heterojunction

https://dx.doi.org/10.1021/acs.analchem.0c02002
Anal. Chem. 2020, 92, 13073−13083

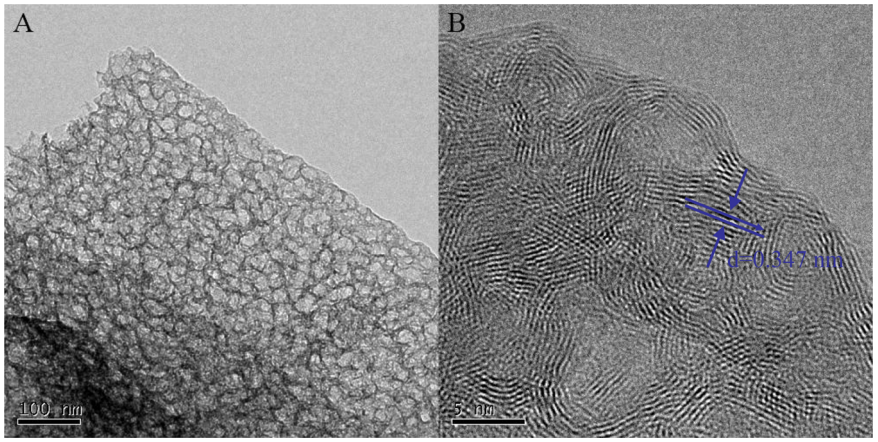

Figure 1. (A) TEM image and (B) HR-TEM image of h-BN nanosheets.

CuS QDs/Co_3O_4 polyhedra-driven multiple signal amplification can enable the h-BN PEC biosensing platform to do the following: (i) the CuS QDs/Co_3O_4 polyhedra can quench the h-BN photoelectrode, resulting in the dramatic decrease of the photocurrent due to the competition of electron donors (AA) and light energy caused by the p-n semiconductor quenching effect; (ii) the CuS QDs/Co_3O_4 polyhedra can act as a peroxidase nanozyme for the catalytic oxidation of 4-chloro-1-naphthol (4-CN) to generate benzo-4-chloro-hexadienone (4-CD) insoluble sediments under a H_2O_2 environment, resulting in an obviously decreased photocurrent. The constructed PEC biosensing platform for the chlorpyrifos assay exhibited good analytical performance with excellent sensitivity. In addition, the CuS QDs/Co_3O_4 polyhedra-enabled h-BN PEC sensing platform exhibits universality and versatility for various analytes via changing the target aptamer sequence, bringing about a bright application in early safety warning, bioanalysis, and clinical diagnosis.

EXPERIMENTAL SECTION

Fabrication of h-BN Nanosheets. Porous h-BN nanosheets were produced according to the method mentioned in our previously published work with slight modifications.[17] Typically, 2.0 g of boric acid and 8.0 g of urea were dissolved in 80 mL of ultrapure water, and the prepared solution was evaporated at 90 °C to obtain a gel. Next, the prepared gel was heated to 900 °C for 6 h under nitrogen gas flow, and then, the white h-BN powders were collected after being cooled to ambient temperature.

Preparation of CuS QDs/Co_3O_4 Polyhedra. The CuS QDs/Co_3O_4 polyhedra were produced by in situ growth. The detailed preparation procedures of ZIF-67 dodecahedra and Co_3O_4 polyhedra are described in the Supporting Information. Co_3O_4 polyhedra powders (100 mg) were uniformly dissolved in 300 mL of ultrapure water by ultrasonication for 1 h. Next, 54 mg of $CuCl_2$ and 80 mg of trisodium citrate were dissolved in the above suspension with magnetic stirring for 5 min. After that, 3 mL of 8 mg mL^{-1} $Na_2S{\cdot}9H_2O$ was slowly dripped into the above suspension and heated to 90 °C for 30 min to obtain CuS QDs/Co_3O_4 polyhedra. In comparison, pure CuS QDs were produced in the same methods without the addition of Co_3O_4 polyhedra. The subsequent preparation process of the SA-labeled CuS QDs/Co_3O_4 polyhedra bioconjugate is described in the Supporting Information.

Construction of PEC Biosensing Platform and PEC Assay. Before modification, the FTO electrode was cleaned ultrasonically in acetone and ethanol/water (v/v, 1:1) for 1 h and then dried with nitrogen gas. First of all, 0.2 mL of 8.0 mg mL^{-1} h-BN suspension was coated on the FTO electrode and dried under an infrared lamp to obtain h-BN/FTO. Next, 20 μL of 0.5% acetic acid containing 1 wt % chitosan (CS) was coated on the surface of the electrode and dried at 60 °C. Subsequently, 20 μL of 2.5 wt % GLD was dropped on h-BN/FTO and kept for 60 min, and then, the nonspecific combined GLD was removed by washing with ultrapure water. Then, 20 μL of 10 mM Tris−HCl buffer (1.0 mM EDTA, 0.2 M NaCl, 0.01 M $MgCl_2$, pH 7.4) containing 1 μM cDNA was dropped on the surface of the h-BN/FTO electrode for 12 h at 4 °C for immobilization. After washing with 10 mM Tris−HCl (pH 7.4) to remove unbound cDNA, 10 μL of 1 wt % bovine serum albumin (BSA) was coated on the cDNA/h-BN/FTO electrode for 1 h to block nonspecific sites. Afterward, the electrode was incubated with the above Tris−HCl buffer containing 20 μL of 1 μM biotin-labeled aptamer (bio-aptamer) for 1 h at 37 °C and then washed. Finally, the PEC aptasensor was produced successfully and stored at 4 °C for further usage.

The modified electrode (aptamer/cDNA/h-BN/FTO) was further incubated with 20 μL of different concentrations (1×10^{-1} to 1×10^{7} ng mL^{-1}) of chlorpyrifos for 80 min at 37 °C. After washing to remove the unfixed aptamer-chlorpyrifos complexes, 20 μL of SA-CuS QDs/Co_3O_4 polyhedra bioconjugate suspension was dropped on the surface of the above electrode and incubated 1 h at 37 °C after washing with 10 mM Tris−HCl (pH 7.4), resulting in the introduction of signal amplifier in the sensing platform due to the specific interaction between SA and biotin. After washing to remove the nonspecific adsorbed SA-CuS QDs/Co_3O_4 polyhedra, the obtained electrode was soaked in 5 mM 4-CN solution (containing 1 mM H_2O_2, pH 4.0) for 20 min to further amplify signal by the MECP reaction. Finally, the PEC assay of chlorpyrifos was carried out in 10 mM Tris−HCl buffer (pH 7.4) containing 0.1 M AA at 0 V.

RESULTS AND DISCUSSION

Characterization of Photoelectric Substrate Material. Transmission electron microscopy (TEM) was used to characterize the morphology and microstructure of porous h-BN nanosheets. As seen from Figure 1A, the prepared h-BN

https://dx.doi.org/10.1021/acs.analchem.0c02002
Anal. Chem. 2020, 92, 13073−13083

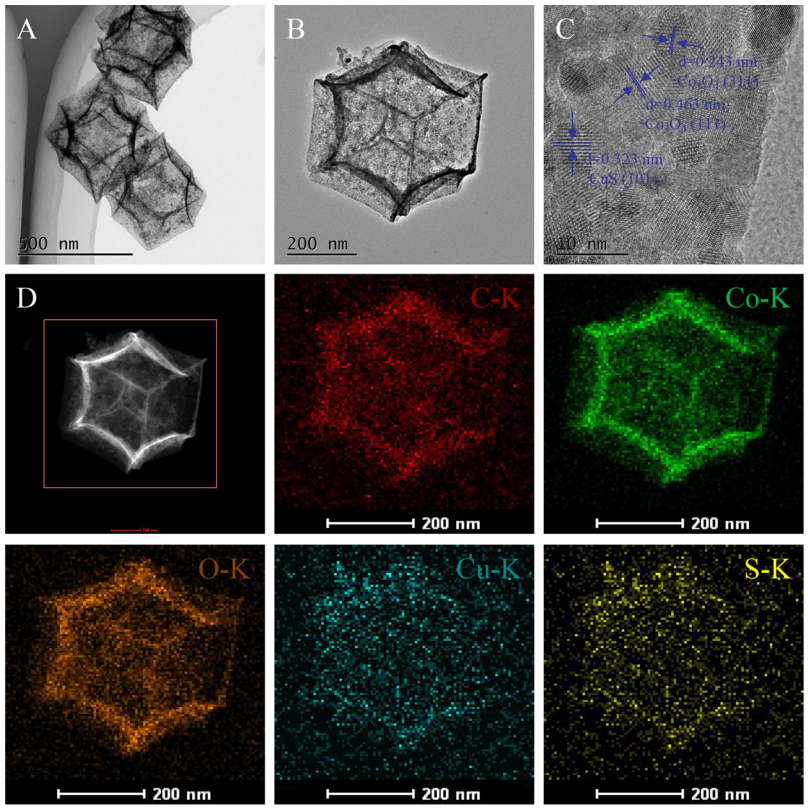

Figure 2. (A, B) TEM images with different magnifications and (C) HR-TEM image of CuS QDs/Co_3O_4 polyhedra. (D) High-angle annular dark-field-scanning transmission electron microscopy (HAADF-STEM) image and EDS mapping of CuS QDs/Co_3O_4 polyhedra.

presented a thin nanosheet structure with abundant pores, which was caused from the released gases during the calcination procedure. The high-resolution TEM (HR-TEM) image (Figure 1B) exhibited a typical layer stacking structure with interlayer distances of 0.347 nm. Moreover, the X-ray diffraction (XRD) analysis (Figure S1A) showed that characteristic diffraction peaks at 42.5 and 25.7° corresponded to the (100) and (002) crystal planes, respectively.[31] In Figure S1B, the X-ray photoelectron spectroscopy (XPS) survey spectrum was employed to measure each element characteristic peaks, which indicated the successful synthesis of h-BN. The N_2 adsorption−desorption isotherms exhibited mesopore distribution (Figure S2), and the specific surface areas and pore volume were 487.67 m^3/g and 0.771 cm^3/g, respectively, which illustrated that the porous h-BN nanosheets were suitable as the photoelectric substrate material to provide extensive active reaction sites.

Characterization of Multiple Signal Amplifier. To investigate the crystallographic structure and phase composition, the XRD analyses of ZIF-67 dodecahedra, Co_3O_4 polyhedra, and CuS QDs/Co_3O_4 polyhedra were carried out. In Figure S3, a series of diffraction peaks of ZIF-67 were corresponding to those in the relevant reference,[32] indicating the successful construction of ZIF-67 dodecahedra. Meanwhile, the characteristic diffraction peaks of Co_3O_4 polyhedra at 19.0, 31.2, 36.9, 44.9, 55.8, 59.5, 65.3, and 78.6° corresponded well to the (111), (220), (311), (400), (422), (511), (440), and (622) planes of pure cubic spinel cobalt oxide, respectively (JCPDS card no.74-2120).[33] The diffraction peaks of CuS QDs/Co_3O_4 polyhedra and Co_3O_4 polyhedra had no obvious difference, which may be attributed to the low concentration of CuS QDs. No redundant diffraction peaks from impurities were observed, indicating that the obtained signal amplifier was of high purity.

The morphologies and structures of ZIF-67 and Co_3O_4 polyhedra were investigated by scanning electron microscopy (SEM). In Figure S4A, the ZIF-67 exhibited a regular rhombic dodecahedral structure with a smooth surface over the whole particle and had an average size of 450 nm. The Co_3O_4 presented a very rough polyhedra shape, and the size average reduces to 300 nm due to the slight contraction caused by the calcination process (Figure S4B). It can be noticeable that, before the air gas heating stage, the thermal treatment in nitrogen gas was to preserve the framework structure because the generated carbon species can act as the extraordinary buffer for preventing the contraction of ZIF-67.[34] The interior structure of CuS QDs/Co_3O_4 polyhedra was further investigated by TEM. The CuS QDs had a uniform distribution on the Co_3O_4 polyhedra surface (Figure 2A, B) with a diameter of 5 nm (from the HR-TEM of CuS QDs; Figure S5), and the HR-TEM image (Figure 2C) exhibited three types of lattice fringes with interplanar spacings of 0.323, 0.463, and 0.243 nm, which corresponded to the (101) lattice plane of CuS QDs and the (111) and (311) lattice planes of Co_3O_4 polyhedra.[35,36] Moreover, the energy-dispersive spectrometry (EDS) mapping (Figure 2D) revealed the existence of C, Co, O, Cu, and S elements. The scans of C, Co, and O further presented the metal−organic framework of Co_3O_4 polyhedra, and those of Cu and S clearly exhibited a random distribution of CuS QDs on the Co_3O_4 polyhedra surface. All the above results indicated the successful synthesis of CuS QDs/Co_3O_4 polyhedra.

XPS analysis was employed to analyze the element compositions of CuS QDs/Co_3O_4 polyhedra.[37] In Figure 3A,

https://dx.doi.org/10.1021/acs.analchem.0c02002
Anal. Chem. 2020, 92, 13073−13083

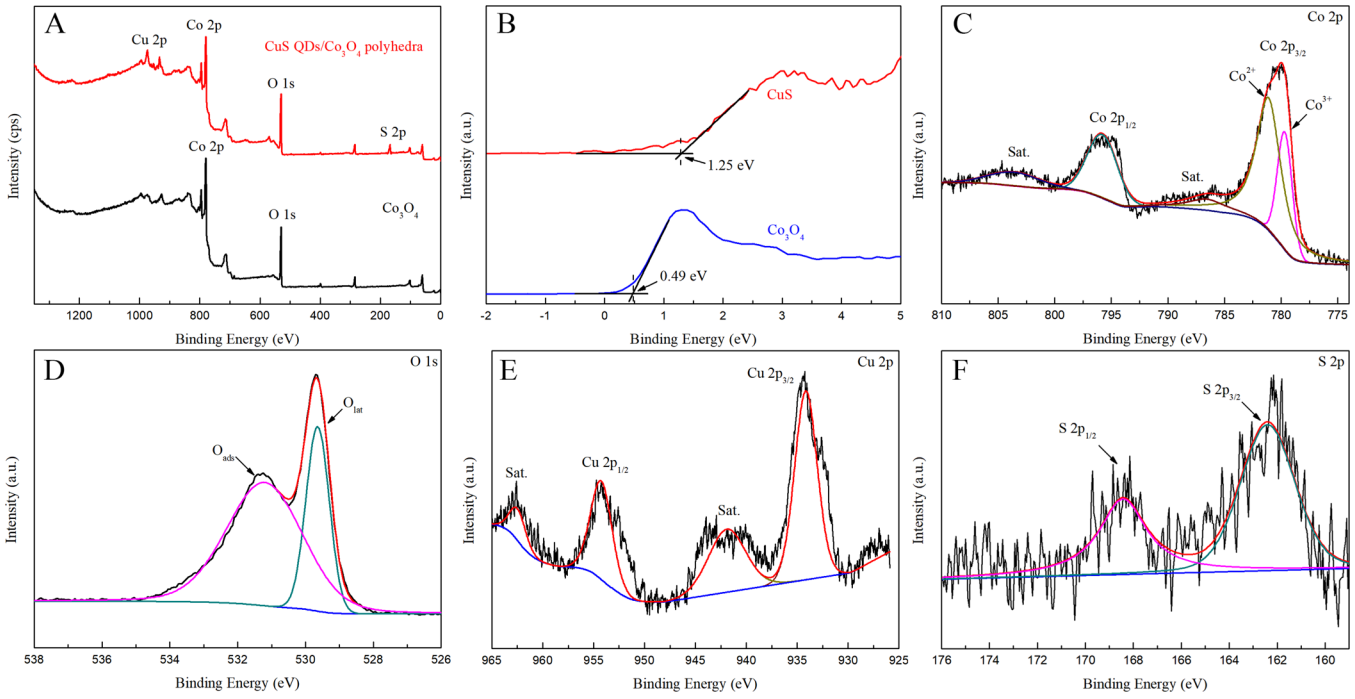

Figure 3. (A) Full-scale XPS spectra of Co_3O_4 and CuS QDs/Co_3O_4 polyhedra. (B) XPS VB spectra of CuS and Co_3O_4. (C−F) High-resolution XPS spectra of CuS QDs/Co_3O_4 polyhedra: Co 2p, O 1s, Cu 2p, and S 2p.

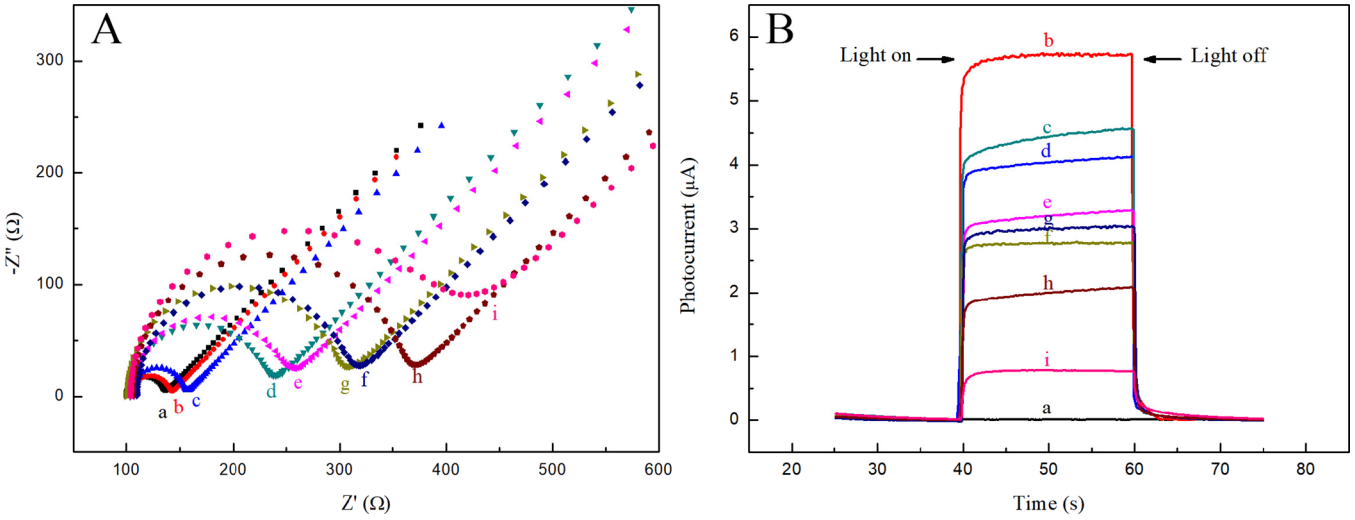

Figure 4. (A) Electrochemical impedance spectra in 5 mM $[Fe(CN)_6]^{3-/4-}$ containing 0.05 M KCl. (B) Photocurrent in 10 mM Tris−HCl (pH 7.4) containing 0.1 M AA of (a) the FTO electrode, (b) h-BN/FTO, (c) h-BN/FTO after coating with CS, (d) cDNA/h-BN/FTO, (e) cDNA/h-BN/FTO after incubation with BSA, (f) aptamer/cDNA/h-BN/FTO, (g) aptamer/cDNA/h-BN/FTO after incubation with 1 ng mL^{-1} chlorpyrifos solution, (h) CuS QDs/Co_3O_4 polyhedra/aptamer/cDNA/h-BN/FTO, and (i) CuS QDs/Co_3O_4 polyhedra/aptamer/cDNA/h-BN/FTO after incubation with 5 mM 4-CN containing 1 mM H_2O_2 for 20 min.

all characteristic diffraction peaks of Co 2p, O 1s, Cu 2p, and S 2p were clearly observed in the survey spectrum of CuS QDs/Co_3O_4 polyhedra, indicating the successful loading of CuS QDs. Moreover, the high-resolution XPS spectrum of individual elements was also analyzed. As depicted in Figure 3C, in addition to two satellite peaks, the binding energy value of 795.8 eV was attributed to the Co $2p_{1/2}$, and the diffraction peaks of Co $2p_{3/2}$ spin orbits at 781.8 and 780.5 eV corresponded to Co^{2+} and Co^{3+}, respectively, indicating the successful preparation of Co_3O_4.[35] Additionally, the surface adsorbed oxygen (O_{ads}) and lattice oxygen species (O_{lat}) were assigned to the binding energy values of 530.8 and 529.6 eV, respectively (Figure 3D).[38] From Figure 3E, it can be observed that two peaks around 953.8 and 933.8 eV were corresponding to Cu $2p_{1/2}$ and Cu $2p_{3/2}$, respectively, revealing that the Cu element mainly existed as a Cu^{2+} state.[39] Furthermore, two apparent satellite peaks were also fitted in Cu 2p regions, and two peaks were located around 169.26 and 162.58 eV, which corresponded to the S $2p_{1/2}$ and S $2p_{3/2}$, respectively, indicating the presence of metal sulfides (Figure 3F). Hence, the formation of CuS can be inferred.

UV−vis DRS spectra were measured to further analyze optical properties. As depicted in Figure S6A, CuS QDs/Co_3O_4 polyhedra exhibited enhanced absorption intensity than

https://dx.doi.org/10.1021/acs.analchem.0c02002
Anal. Chem. 2020, 92, 13073−13083

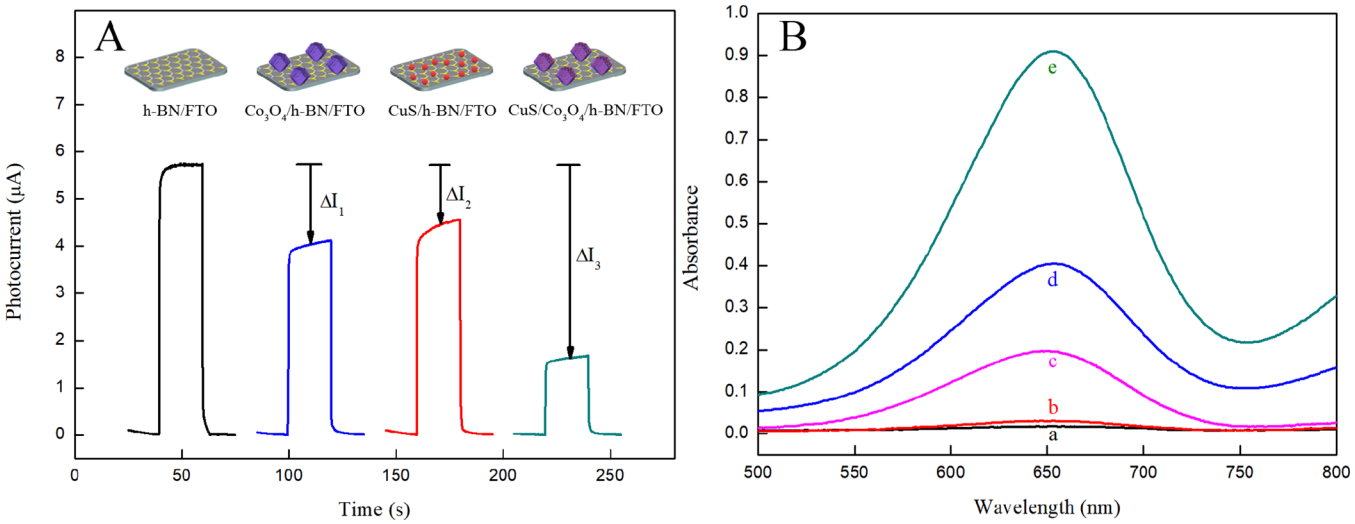

Figure 5. (A) Photocurrent responses of h-BN/FTO, Co_3O_4 polyhedra/h-BN/FTO, CuS polyhedra/h-BN/FTO, and CuS QDs/Co_3O_4 polyhedra/h-BN/FTO. (B) UV−vis absorption spectra: (a) TMB, (b) TMB-H_2O_2, (c) CuS QDs/Co_3O_4 polyhedra-TMB, (d) Co_3O_4-TMB-H_2O_2, and (e) CuS QDs/Co_3O_4 polyhedra-TMB-H_2O_2 in the sodium acetate buffer (pH 4.0).

pure Co_3O_4 under visible light, which was attributed to the excellent light absorption capacity of CuS QDs. Moreover, the band gap can be estimated by the Kubelka−Munk method on the basis of the following formula[40]

$$\alpha h\nu = A(h\nu - E_g)^{n/2} \quad (1)$$

where α, h, ν, A and E_g represent the absorption coefficient, Planck constant, light frequency, a constant, and band gap energy, respectively. For Co_3O_4 and CuS, the n value is 4, which depends on the direct or indirect types of semiconductors. In Figure S6B, Tauc's plots show that the band gap values of Co_3O_4 and CuS are 2.12 and 1.90 eV, which were consistent with the relevant literature.[27,41] To investigate the charge transfer in detail, the valence band (VB) was measured by XPS VB spectra. In Figure 3B, the VB positions of Co_3O_4 and CuS were +0.49 and +1.25 eV (vs NHE, normal hydrogen electron), respectively. Therefore, the conduction band (CB) potentials of Co_3O_4 and CuS could be calculated to be −1.63 and −0.65 eV, respectively.

The above results revealed that the prepared CuS QDs/Co_3O_4 polyhedra had remarkable photoelectric performance and could be utilized for PEC biosensing.

EIS and PEC Characterization of the PEC Biosensing Platform. To investigate the step-by-step modification procedure of the biosensing platform, electrochemical impedance spectroscopy (EIS) was conducted, and the semicircle diameter revealed the interfacial charge−transfer resistance (R_{ct}). In Figure 4A, h-BN/FTO (curve b) presented a modest increased R_{ct} value than the bare FTO electrode (curve a), which should be assigned to the inherent property of the semiconductor. After the orderly modification of CS, cDNA, BSA, and aptamer on the h-BN/FTO electrode, the R_{ct} increased successively (curves c to f) due to the weak conductive property and impediment effect on the electron transfer process. As expected, after being incubated with 1 ng mL^{-1} chlorpyrifos, the aptamer fell off from the electrode surface due to the strong affinity of aptamer-chlorpyrifos complexes, leading to a slight decreased R_{ct} (curve g). Afterward, the CuS QDs/Co_3O_4 polyhedra were drawn into the biosensing platform because of the specific reaction between biotin and SA; an increased R_{ct} value was found (curve h) on account of its steric hindrance. Finally, a sharply increased R_{ct} could be observed (curve i) after incubating with 4-CN solution containing H_2O_2. The phenomenon could be explained that the formation of the 4-CD insoluble precipitate blocked the charge transfer of $[Fe(CN)_6]^{3-/4-}$.

The stepwise fabrication procedure of the constructed electrode was further characterized by PEC measurement. As shown in Figure 4B, the bare FTO electrode had almost no photocurrent (curve a), while the h-BN/FTO electrode showed the largest anodic photocurrent with an ignorable background signal (curve b) due to the excellent photoelectric conversion efficiency. Subsequently, the photocurrent signal decreased in turn with the successive modification of CS, cDNA, BSA, and aptamer on the h-BN/FTO electrode (curves c to f), which was consistent with the results of EIS. The results could be explained that the linker molecule and biomolecule owned poor biological conductivity and high steric hindrance, blocking the electron transfer from AA (as electron donors) to the electrode surface. However, the photocurrent response increased slightly (curve g) after being incubated with 1 ng mL^{-1} chlorpyrifos, which could be attributed to that of the strong binding capacity between chlorpyrifos and the aptamer, leading to the shedding of aptamer from the electrode. When the above electrode was incubated with SA-CuS QDs/Co_3O_4 polyhedra bioconjugate solution, the photocurrent intensity decreased obviously (curve h), which was assigned to its p-n quenching effect for the effective competition of electron donors and exciting light. Last, after incubation with 4-CN solution containing H_2O_2, the photocurrent signal decreased dramatically (curve i); the generated insoluble precipitate 4-CD could hinder electron transfer from AA (electron donor) to the electrode surface. The EIS and PEC results demonstrated that the CuS QDs/Co_3O_4 polyhedra-based h-BN PEC biosensing platform can be used for the chlorpyrifos assay.

Evaluation on the Superiority of CuS QDs/Co_3O_4 Polyhedra. To compare the difference with and without the signal amplifications, the comparison experiment was conducted. As shown in Figure S10, the ΔI_2 (photocurrent difference value with multiple signal amplifications) was about

https://dx.doi.org/10.1021/acs.analchem.0c02002
Anal. Chem. 2020, 92, 13073−13083

Scheme 2. Mechanism of CuS QDs/Co_3O_4 Polyhedra-Driven Multiple Signal Amplifications (Red Curve: p-n Semiconductor Quenching Effect; Blue Curve: Mimetic Enzymatic Catalytic Precipitation Effect)

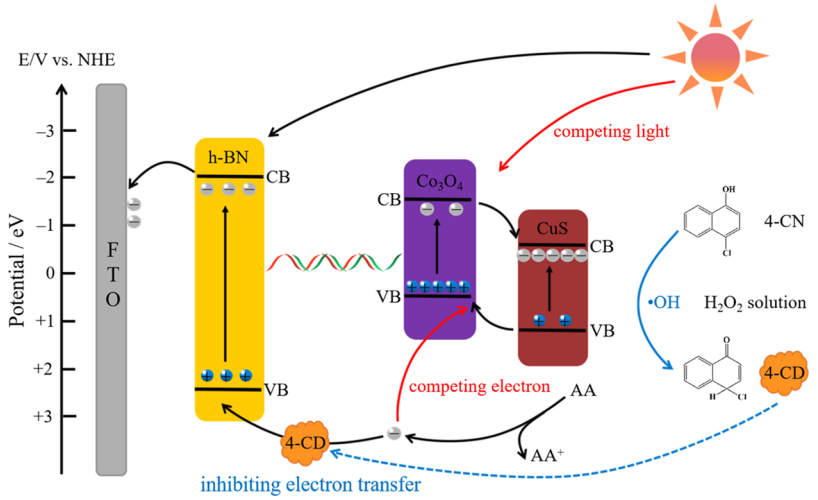

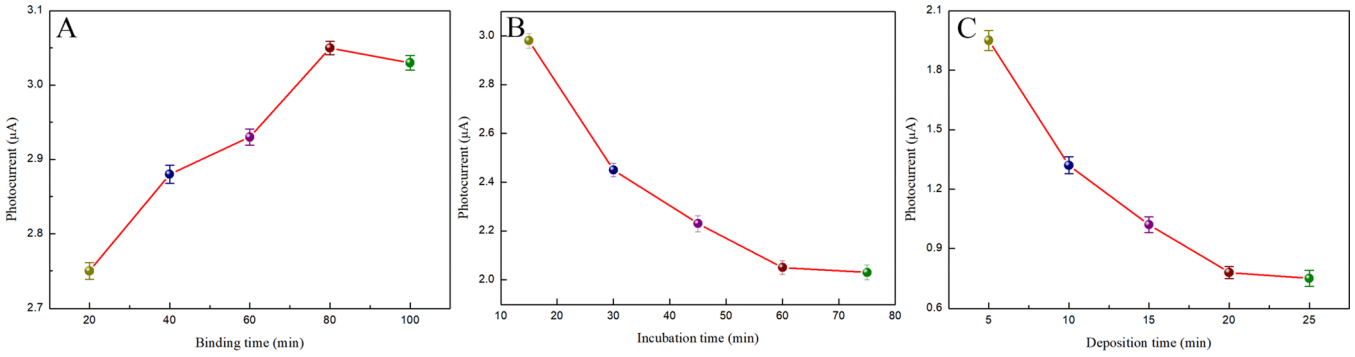

Figure 6. Effects of (A) the binding time of chlorpyrifos, (B) the incubation time of CuS QDs/Co_3O_4 polyhedra, and (C) the deposition time of 4-CN on the photocurrents of the PEC biosensor.

20 times more than ΔI_1 (photocurrent difference value without signal amplification), which illustrated that the CuS QDs/Co_3O_4 polyhedra have excellent signal amplification capability.

To further investigate the quenching ability of CuS QDs/Co_3O_4 polyhedra in the h-BN PEC biosensing platform, the comparison study was conducted by contrasting the photocurrent signal of different signal amplifiers under the same experimental conditions (same as the above PEC measurement). As shown in Figure 5A, the h-BN/FTO showed the largest anodic photocurrent, which corresponded to the above results. Both the photocurrent value of Co_3O_4/h-BN/FTO and CuS/h-BN/FTO decreased due to the p-n semiconductor quenching effect. What is more, it is noted that the photocurrent signal of CuS/Co_3O_4/h-BN/FTO decreased obviously and the ΔI_3 was significantly larger than the sum values of ΔI_1 and ΔI_2, which was ascribed to the formation of the CuS QDs/Co_3O_4 polyhedra p-type heterojunction. Based on the CB and VB position of Co_3O_4 and CuS, the possible mechanism of electron transfer could be inferred as follows: the electrons on CB of Co_3O_4 easily transferred to the CB of CuS, and the holes on VB of CuS flowed into the VB of Co_3O_4 due to the energy band match in the heterojunction system, which inhibited the recombination of electron−hole pairs and promoted the competition of electron donors (AA) and exciting light, resulting in a dramatic enhancement of the p-n semiconductor quenching effect (as shown in Scheme 2, see the red curve).

In addition, CuS QDs/Co_3O_4 polyhedra possess mimic nanozyme activity and the possible mechanism of the mimetic enzymatic catalytic precipitation effect could be inferred as follows:[24,42] CuS QDs/Co_3O_4 polyhedra with peroxidase-like activity may produce abundant hydroxyl radicals (•OH) in the existence of H_2O_2, and then, the generated •OH oxidated 4-CN to insoluble precipitate 4-CD, resulting in inhibiting the electron transfer (as shown in Scheme 2, see the blue curve). To further evaluate the peroxidase-like activity of CuS QDs/Co_3O_4 polyhedra, the catalytic oxidation reaction was measured by utilizing the chromogenic substrate TMB under an H_2O_2 environment.[43] As shown in Figure 5B, when there is no addition of nanozyme, there are no absorption peaks (curves a and b), regardless of the existence of H_2O_2. When only TMB and CuS QDs/Co_3O_4 polyhedra exist, the absorption peak (curve c) slightly increased, which could be attributed to the oxidase-like activity of Co_3O_4 itself.[44] After the introduction of Co_3O_4 or CuS QDs/Co_3O_4 polyhedra in sodium acetate buffer (containing TMB and H_2O_2, pH 4.0), two obvious absorption peaks could be observed (curves d and e), indicating that both Co_3O_4 and CuS QDs/Co_3O_4 polyhedra possessed excellent peroxidase-like abilities. In addition, the peak intensity of CuS QDs/Co_3O_4 polyhedra (curve e) is significantly higher than pure Co_3O_4 (curve d), which may be ascribed to the CuS QDs' peroxidase-like activity and the enhanced specific surface areas with the loading of quantum dots.

https://dx.doi.org/10.1021/acs.analchem.0c02002
Anal. Chem. 2020, 92, 13073−13083

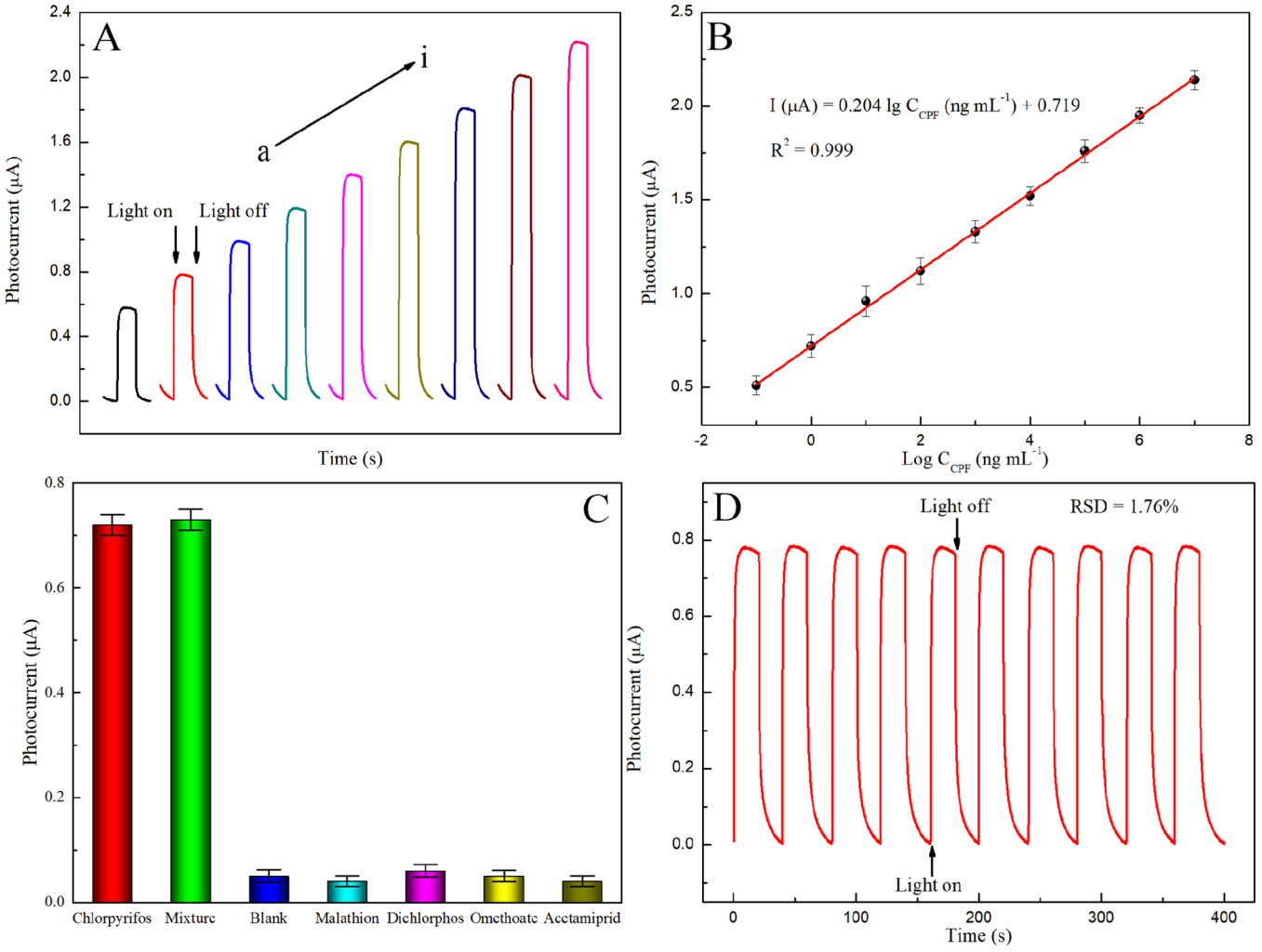

Figure 7. (A) Photocurrent signals and (B) linear regression curve of the PEC biosensing platform for chlorpyrifos detection with various concentrations (from a to i: 1×10^{-1} to 1×10^{7} ng mL^{-1}). (C) Selectivity of the developed PEC biosensing platform: chlorpyrifos, mixture, blank, malathion, dichlorphos, omethoate, and acetamiprid. (D) Stability of the fabricated PEC biosensing platform incubated with 1 ng mL^{-1} chlorpyrifos.

These comparison results above reveal that CuS QDs/Co_3O_4 polyhedra can be utilized as a preferable signal amplifier in the h-BN PEC biosensing platform.

Optimization of Experimental Conditions for the PEC Aptasensor. So as to attain outstanding sensitivity and the optimum state of this PEC biosensing platform for chlorpyrifos detection, some important factors, including the binding time of chlorpyrifos, the incubation time of CuS QDs/Co_3O_4 polyhedra, and the deposition time of 4-CN, were optimized. Figure 6A shows that the photocurrent increased along with the binding time of chlorpyrifos increased from 20 to 100 min and reached a plateau at 80 min, implying that the binding reaction reached saturation. Thus, 80 min was selected as the optimal binding time of chlorpyrifos. Moreover, the incubation time of CuS QDs/Co_3O_4 polyhedra was also an important factor (in Figure 6B). With the increase of the incubation time, more CuS QDs/Co_3O_4 polyhedra were attached to the h-BN electrode, which could compete for light irradiation and electron donor, causing the photocurrent to decrease and remain stable at 1 h. Hence, 1 h was taken as the optimum incubation time of CuS QDs/Co_3O_4 polyhedra. As depicted in Figure 6C, with the increase of the deposition time of 4-CN, the photocurrent signal decreased and reached a plateau at 20 min because abundant 4-CD precipitates were deposited due to the catalytic deposition reaction. Therefore, 20 min served as the optimal deposition time. In addition, as we know, either a positive- or negative-applied potential probably does some damage to the stability of the biosensing system and enhances the background signal,[45,46] so 0 V was selected to develop a self-powered PEC biosensing platform for the chlorpyrifos assay.

Performance of the PEC Aptasensor. To assess the performance of the PEC biosensor, the photocurrent responses were measured under a series of different concentrations (1×10^{-1} to 1×10^{7} ng mL^{-1}) of chlorpyrifos under the optimized conditions. From Figure 7A, the photocurrent accordingly raised as increase concentration of chlorpyrifos, corresponding to the weakening multiple signal amplifications of CuS QDs/Co_3O_4 polyhedra. In Figure 7B, the linear relationship between the logarithm of chlorpyrifos concentration and the photocurrent signal could be observed with a linear equation of I (μA) = 0.204 lg C_{CPF} (ng mL^{-1}) + 0.719 (R^2 = 0.999) and a limit of detection (LOD) of 0.34 pg mL^{-1} (the calculation of LOD was according to the formula $3\sigma/s$[47] where σ is the standard deviation of the blank samples and s is the slope of the calibration curve). In contrast with other techniques

https://dx.doi.org/10.1021/acs.analchem.0c02002
Anal. Chem. 2020, 92, 13073−13083

published previously, the proposed PEC biosensing platform presented a wider detection range and lower detection limit for the chlorpyrifos assay (Table S1).

Selectivity, Reproducibility, and Stability. The selectivity is a crucial parameter for estimating potential application of the biosensing platform in a complex environment. Therefore, malathion, dichlorphos, omethoate, and acetamiprid were considered as interference substances to assess the PEC selectivity of the developed aptasensor. As shown in Figure 7C, four interferents (5 ng mL^{-1}) were observed with low photocurrent values, which were nearly identical to the blank group. Furthermore, a significantly increased photocurrent was also observed in the mixture sample containing 1 ng mL^{-1} chlorpyrifos and four interference substances (each, 5 ng mL^{-1}), and this photocurrent signal was slightly smaller than that in the chlorpyrifos solution (the same concentration) without any interferent. These results indicated that the interference effect could be ignored, and the constructed PEC biosensing platform possessed an excellent selectivity.

Additionally, five independent electrodes were incubated in chlorpyrifos of the same concentration (1 ng mL^{-1}) under the same conditions, and photocurrent signals were nearly identical with a relative standard deviation (RSD) of 3.2%, performing a gratifying reproducibility. On the other hand, the photocurrent signals of the developed biosensor were steady without noticeable changes (RSD = 1.76%) under the 10 on−off irradiation cycles, which illustrated a satisfactory stability (Figure 7D). In addition, when the PEC biosensing platform was kept at 4 °C for 1 month under dark conditions, the photocurrent intensity still can remain 98.7% of its initial value, giving a nice long-term stability.

Recovery Assay in Real Samples. To assess the practicability of the signal amplifier CuS QDs/Co_3O_4 polyhedra based on the h-BN PEC aptasensor, different concentrations (1, 10, and 100 ng mL^{-1}) of chlorpyrifos were spiked into river water, an apple, and a lettuce, respectively. The detailed real sample preparation procedure is described in the Supporting Information. The related results are exhibited in Table S2, and the recoveries were 98.27−103.47% with an RSD value in the range of 1.53−2.68%, demonstrating an excellent recovery and promising applicability for the chlorpyrifos assay in complex environment conditions.

CONCLUSIONS

In summary, a novel h-BN photoeletrochemical biosensing platform without modification was activated based on CuS QDs/Co_3O_4 polyhedra-driven multiple signal amplifications. The CuS QDs/Co_3O_4 polyhedra, as a newly signal amplifier, can trigger the p-n semiconductor quenching effect and mimetic enzymatic catalytic precipitation effect for the available enhancement of sensitivity. The developed PEC biosensing platform for the chlorpyrifos assay presents a wide linear range from 1×10^{-1} to 1×10^{7} ng mL^{-1} and a low detection limit of 0.34 pg mL^{-1} and exhibits outstanding selectivity, satisfactory reproducibility, and stability. In addition, the CuS QDs/Co_3O_4 polyhedra-enabled h-BN PEC biosensing platform exhibits universality for various analytes via replacing the corresponding target aptamer sequence. Significantly, the activated h-BN PEC biosensing platform can overcome the issues of high background signal, instability, and poor reproducibility caused by the complex modification of photoactive substrate materials in conventional PEC biosensors. The signal amplifier-driven PEC biosensing platform strategy provides a remarkable inspiration and valuable reference for the development of the PEC biosensor with a low background signal and outstanding sensitivity and has bright application in early safety warning, bioanalysis, and clinical diagnosis.

ASSOCIATED CONTENT

Supporting Information

The Supporting Information is available free of charge at https://pubs.acs.org/doi/10.1021/acs.analchem.0c02002.

Reagents and materials, instruments, some material preparation procedures, performance of the aptamer, and real sample preparation; XRD and XPS survey spectrum of h-BN (Figure S1); N_2 adsorption−desorption isotherms of h-BN (Figure S2); XRD patterns of ZIF-67 and CuS QDs/Co_3O_4 polyhedra (Figure S3); SEM images of ZIF-67 dodecahedra and Co_3O_4 polyhedra (Figure S4); HR-TEM images of CuS QDs (Figure S5); UV−vis diffuse reflectance spectra of CuS QDs/Co_3O_4 polyhedra (Figure S6); electrospray ionization mass spectrum of the aptamer and cDNA (Figure S7); DNA gel electrophoresis (Figure S8); surface plasmon resonance assay (Figure S9); photocurrent responses with and without multiple signal amplifications (Figure S10); comparison of different methods for chlorpyrifos detection (Table S1); and recovery assay for chlorpyrifos in real samples (Table S2) (PDF)

AUTHOR INFORMATION

Corresponding Authors

Lin Tang − *College of Environmental Science and Engineering, Hunan University, Changsha 410082, China; Ministry of Education, Key Laboratory of Environmental Biology and Pollution Control (Hunan University), Changsha, Hunan 410082, China;* orcid.org/0000-0001-6996-7955; Phone: +86-731-88822829; Email: tanglin@hnu.edu.cn; Fax: +86-731-88823701

Guangming Zeng − *College of Environmental Science and Engineering, Hunan University, Changsha 410082, China; Ministry of Education, Key Laboratory of Environmental Biology and Pollution Control (Hunan University), Changsha, Hunan 410082, China;* orcid.org/0000-0002-4230-7647; Email: zgming@hnu.edu.cn

Authors

Jisui Tan − *College of Environmental Science and Engineering, Hunan University, Changsha 410082, China; Ministry of Education, Key Laboratory of Environmental Biology and Pollution Control (Hunan University), Changsha, Hunan 410082, China*

Bo Peng − *College of Environmental Science and Engineering, Hunan University, Changsha 410082, China; Ministry of Education, Key Laboratory of Environmental Biology and Pollution Control (Hunan University), Changsha, Hunan 410082, China*

Yue Lu − *College of Environmental Science and Engineering, Hunan University, Changsha 410082, China; Ministry of Education, Key Laboratory of Environmental Biology and Pollution Control (Hunan University), Changsha, Hunan 410082, China*

https://dx.doi.org/10.1021/acs.analchem.0c02002
Anal. Chem. 2020, 92, 13073−13083

Jiajia Wang − *College of Environmental Science and Engineering, Hunan University, Changsha 410082, China; Ministry of Education, Key Laboratory of Environmental Biology and Pollution Control (Hunan University), Changsha, Hunan 410082, China*

Xilian Ouyang − *College of Environmental Science and Engineering, Hunan University, Changsha 410082, China; Ministry of Education, Key Laboratory of Environmental Biology and Pollution Control (Hunan University), Changsha, Hunan 410082, China*

Xu Zhu − *College of Environmental Science and Engineering, Hunan University, Changsha 410082, China; Ministry of Education, Key Laboratory of Environmental Biology and Pollution Control (Hunan University), Changsha, Hunan 410082, China*

Yu Chen − *College of Environmental Science and Engineering, Hunan University, Changsha 410082, China; Ministry of Education, Key Laboratory of Environmental Biology and Pollution Control (Hunan University), Changsha, Hunan 410082, China*

Haopeng Feng − *College of Environmental Science and Engineering, Hunan University, Changsha 410082, China; Ministry of Education, Key Laboratory of Environmental Biology and Pollution Control (Hunan University), Changsha, Hunan 410082, China*

Complete contact information is available at: https://pubs.acs.org/10.1021/acs.analchem.0c02002

Notes

The authors declare no competing financial interest.

■ ACKNOWLEDGMENTS

The study was supported by projects 51579096 and 51521006, supported by the National Natural Science Foundation of China, the National Innovative Talent Promotion Program of China (2017RA2088), the Funds for Innovative Province Construction of Hunan Province of China (2019RS3012), and the National Program for Support of Top-North Young Professionals of China (2012).

■ REFERENCES

(1) Chu, Y.; Deng, A.-P.; Wang, W.; Zhu, J.-J. *Anal. Chem.* **2019**, *91*, 3619−3627.
(2) Haddour, N.; Chauvin, J.; Gondran, C.; Cosnier, S. *J. Am. Chem. Soc.* **2006**, *128*, 9693−9698.
(3) Zhao, W.-W.; Xu, J.-J.; Chen, H.-Y. *Chem. Rev.* **2014**, *114*, 7421−7441.
(4) Zeng, R.; Luo, Z.; Su, L.; Zhang, L.; Tang, D.; Niessner, R.; Knopp, D. *Anal. Chem.* **2019**, *91*, 2447−2454.
(5) Rajwar, D.; Ammanath, G.; Cheema, J. A.; Palaniappan, A.; Yildiz, U. H.; Liedberg, B. *ACS Appl. Mater. Interfaces* **2016**, *8*, 8349−8357.
(6) Hatchett, D. W.; Josowicz, M. *Chem. Rev.* **2008**, *108*, 746−769.
(7) Dai, W.-X.; Zhang, L.; Zhao, W.-W.; Yu, X.-D.; Xu, J.-J.; Chen, H.-Y. *Anal. Chem.* **2017**, *89*, 8070−8078.
(8) Lupan, O.; Postica, V.; Wolff, N.; Polonskyi, O.; Duppel, V.; Kaidas, V.; Lazari, E.; Ababii, N.; Faupel, F.; Kienle, L.; Adelung, R. *Small* **2017**, *13*, 1602868.
(9) Gao, C.; Yu, H.; Zhang, L.; Zhao, Y.; Xie, J.; Li, C.; Cui, K.; Yu, J. *Anal. Chem.* **2020**, *92*, 2902−2906.
(10) Wan, J.; Lacey, S. D.; Dai, J.; Bao, W.; Fuhrer, M. S.; Hu, L. *Chem. Soc. Rev.* **2016**, *45*, 6742−6765.
(11) Zeng, R.; Zhang, L.; Su, L.; Luo, Z.; Zhou, Q.; Tang, D. *Biosens. Bioelectron.* **2019**, *133*, 100−106.
(12) Wang, M.; Yin, H.; Zhou, Y.; Sui, C.; Wang, Y.; Meng, X.; Waterhouse, G. I. N.; Ai, S. *Biosens. Bioelectron.* **2019**, *128*, 137−143.
(13) Feng, C.; Tang, L.; Deng, Y.; Zeng, G.; Wang, J.; Liu, Y.; Chen, Z.; Yu, J.; Wang, J. *Appl. Catal., B* **2019**, *256*, 117827.
(14) Weng, Q.; Wang, B.; Wang, X.; Hanagata, N.; Li, X.; Liu, D.; Wang, X.; Jiang, X.; Bando, Y.; Golberg, D. *ACS Nano* **2014**, *8*, 6123−6130.
(15) Weng, Q.; Kvashnin, D. G.; Wang, X.; Cretu, O.; Yang, Y.; Zhou, M.; Zhang, C.; Tang, D.-M.; Sorokin, P. B.; Bando, Y.; Golberg, D. *Adv. Mater.* **2017**, *29*, 1700695.
(16) Zhang, K. X.; Su, H.; Wang, H. H.; Zhang, J. J.; Zhao, S. Y.; Lei, W.; Wei, X.; Li, X. H.; Chen, J. S. *Adv. Sci.* **2018**, *5*, 1800062.
(17) Tan, J.; Peng, B.; Tang, L.; Feng, C.; Wang, J.; Yu, J.; Ouyang, X.; Zhu, X. *Biosens. Bioelectron.* **2019**, *142*, 111546.
(18) Wang, S.; Wang, F.; Fu, C.; Sun, Y.; Zhao, J.; Li, N.; Liu, Y.; Ge, S.; Yu, J. *Anal. Chem.* **2020**, *92*, 7604−7611.
(19) Yang, R.; Zou, K.; Li, Y.; Meng, L.; Zhang, X.; Chen, J. *Anal. Chem.* **2018**, *90*, 9480−9486.
(20) Li, M.-J.; Zheng, Y.-N.; Liang, W.-B.; Yuan, R.; Chai, Y.-Q. *ACS Appl. Mater. Interfaces* **2017**, *9*, 42111−42120.
(21) Zhu, X.; Gao, L.; Tang, L.; Peng, B.; Huang, H.; Wang, J.; Yu, J.; Ouyang, X.; Tan, J. *Biosens. Bioelectron.* **2019**, *146*, 111756.
(22) Gao, L.; Zhuang, J.; Nie, L.; Zhang, J.; Zhang, Y.; Gu, N.; Wang, T.; Feng, J.; Yang, D.; Perrett, S.; Yan, X. *Nat. Nanotechnol.* **2007**, *2*, 577−583.
(23) Song, Y.; Qu, K.; Zhao, C.; Ren, J.; Qu, X. *Adv. Mater.* **2010**, *22*, 2206−2210.
(24) Kandula, S.; Jeevanandam, P. *RSC Adv.* **2015**, *5*, 5295−5306.
(25) Kaneti, Y. V.; Dutta, S.; Hossain, M. S. A.; Shiddiky, M. J. A.; Tung, K.-L.; Shieh, F.-K.; Tsung, C.-K.; Wu, K. C.-W.; Yamauchi, Y. *Adv. Mater.* **2017**, *29*, 1700213.
(26) Lü, Y.; Zhan, W.; He, Y.; Wang, Y.; Kong, X.; Kuang, Q.; Xie, Z.; Zheng, L. *ACS Appl. Mater. Interfaces* **2014**, *6*, 4186−4195.
(27) Lai, C.; Zhang, M.; Li, B.; Huang, D.; Zeng, G.; Qin, L.; Liu, X.; Yi, H.; Cheng, M.; Li, L.; Chen, Z.; Chen, L. *Chem. Eng. J.* **2019**, *358*, 891−902.
(28) Huang, D.; Wang, L.; Zhan, Y.; Zou, L.; Ye, B. *Biosens. Bioelectron.* **2019**, *140*, 111358.
(29) Jiao, Y.; Huang, Q.; Wang, J.; He, Z.; Li, Z. *Appl. Catal., B* **2019**, *247*, 124−132.
(30) Putri, L. K.; Ng, B.-J.; Ong, W.-J.; Lee, H. W.; Chang, W. S.; Mohamed, A. R.; Chai, S.-P. *Appl. Catal., B* **2020**, 118592.
(31) Wang, L.; Ni, S.-Q.; Guo, C.; Qian, Y. *J. Mater. Chem. A* **2013**, *1*, 6379−6387.
(32) Banerjee, R.; Phan, A.; Wang, B.; Knobler, C.; Furukawa, H.; O'Keeffe, M.; Yaghi, O. M. *Science* **2008**, *319*, 939−943.
(33) Wu, R.; Qian, X.; Rui, X.; Liu, H.; Yadian, B.; Zhou, K.; Wei, J.; Yan, Q.; Feng, X.-Q.; Long, Y.; Wang, L.; Huang, Y. *Small* **2014**, *10*, 1932−1938.
(34) Xu, X.; Cao, R.; Jeong, S.; Cho, J. *Nano Lett.* **2012**, *12*, 4988−4991.
(35) Liu, D.; Chen, D.; Li, N.; Xu, Q.; Li, H.; He, J.; Lu, J. *Small* **2019**, *15*, 1902291.
(36) Fang, Y.; Guan, B. Y.; Luan, D.; Lou, X. W. (. D. *Am. Ethnol.* **2019**, *131*, 7821−7825.
(37) Peng, B.; Tang, L.; Zeng, G.; Fang, S.; Ouyang, X.; Long, B.; Zhou, Y.; Deng, Y.; Liu, Y.; Wang, J. *Biosens. Bioelectron.* **2018**, *121*, 19−26.
(38) Wang, X.; Li, X.; Mu, J.; Fan, S.; Chen, X.; Wang, L.; Yin, Z.; Tadé, M.; Liu, S. *ACS Appl. Mater. Interfaces* **2019**, *11*, 41988−41999.
(39) Tang, Y.; Chai, Y.; Liu, X.; Li, L.; Yang, L.; Liu, P.; Zhou, Y.; Ju, H.; Cheng, Y. *Biosens. Bioelectron.* **2018**, *117*, 224−231.
(40) Tang, L.; Ouyang, X.; Peng, B.; Zeng, G.; Zhu, Y.; Yu, J.; Feng, C.; Fang, S.; Zhu, X.; Tan, J. *Nanoscale* **2019**, *11*, 12198−12209.
(41) Zhang, P.; Wang, T.; Chang, X.; Zhang, L.; Gong, J. *Angew. Chem., Int. Ed.* **2016**, *55*, 5851−5855.
(42) Li, Y.-Z.; Li, T.-T.; Chen, W.; Song, Y.-Y. *ACS Appl. Mater. Interfaces* **2017**, *9*, 29881−29888.

(43) Wu, Y.; Li, G.; Zou, L.; Lei, S.; Yu, Q.; Ye, B. *Sens. Actuators, B* **2018**, *259*, 372−379.
(44) Zhuang, Y.; Zhang, X.; Chen, Q.; Li, S.; Cao, H.; Huang, Y. *Mater. Sci. Eng. C* **2019**, *94*, 858−866.
(45) Fu, Y.; Zou, K.; Liu, M.; Zhang, X.; Du, C.; Chen, J. *Anal. Chem.* **2019**, *92*, 1189−1196.
(46) Yang, H.; Hu, M.; Li, Z.; Zhao, P.; Xie, L.; Song, X.; Yu, J. *Anal. Chem.* **2019**, *91*, 14577−14585.
(47) Çakıroğlu, B.; Özacar, M. *Biosens. Bioelectron.* **2018**, *119*, 34−41.

https://dx.doi.org/10.1021/acs.analchem.0c02002
Anal. Chem. 2020, 92, 13073−13083